RSC Advances

PAPER

View Article Online
View Journal | View Issue

Cite this: *RSC Adv.*, 2025, **15**, 16643

Mechanistic insights into the visible light photocatalytic activity of g-C_3N_4/$Bi_2O_2CO_3$–Bi_4O_7 composites for rhodamine B degradation and hexavalent chromium reduction†

Aleena Majeed,[a] Samna Hassan,[a] Musarrat Zahra,[a] Iqra Rafique,[b] Sajid Iqbal,[c] Munib Ahmad Shafiq,[d] Rashid Nazir Qureshi,[d] Ramzan Akhtar,[e] Muhammad Rehan,[f] Mohsin Ali Raza Anjum,[e] Sheeraz Mehboob,[e] Jaweria Ambreen,*[ag] Jae Ho Yun*[h] and Muhammad Saifullah*[e]

The two-dimensional layered structure of g-C_3N_4 (GCN) has drawn a lot of attention in the field of photocatalysis due to its good thermochemical stability, large surface area, and environmental friendliness. A wide bandgap of GCN restricts its absorption to UV light and a limited portion of visible light; therefore, its bandgap engineering by coupling it with a suitable semiconductor can offer the utilization of a wider spectrum of incident light and a lower electron–hole recombination rate. In this study, GCN is coupled with mixed-phase $Bi_2O_2CO_3$–Bi_4O_7 (BO) in different weight percentages (wt%) to find the optimal loading of BO for maximum photocatalytic degradation. The XRD analysis confirms the preparation of GCN, BO, and g-C_3N_4/$Bi_2O_2CO_3$–Bi_4O_7 composites. The g-C_3N_4/$Bi_2O_2CO_3$–Bi_4O_7 composite with 24 wt% of BO (CN/BO-24) demonstrates 92.3% rhodamine B (RhB) dye degradation in 25 min under visible light irradiation, which is considerably higher compared with the corresponding % degradation realized with pristine GCN (73.4%) and BO (9.4%). The improved performance of the composite with optimal loading of BO is attributed to the reduced recombination rate of photo-generated electrons and holes, as confirmed by photoluminescence analysis, and utilization of a wider spectrum of incident light. Photo-degradation experiments performed with different scavengers reveal that peroxide radicals and holes play a decisive role in the degradation of RhB using the best composite sample (CN/BO-24). The potential of the CN/BO-24 ternary composite for the photoreduction of Cr(VI) is also explored. The fabricated composite holds promising potential in water treatment and environmental remediation.

Received 10th February 2025
Accepted 6th May 2025

DOI: 10.1039/d5ra00969c

rsc.li/rsc-advances

1. Introduction

Drastic environmental degradation has been affecting the lives of billions of people worldwide in recent times due to rapid industrial development. This advancement has led to the use of many new chemicals in a diverse range of commercial applications. Organic dyes are one of these compounds used on a massive scale in the textile sector. These dyes are crucial to different sectors and, thereby, have become an inevitable component of industrial effluents. It has been estimated that over 11% of the 450 000 tons of organic dyes synthesized globally each year are lost in effluents throughout the manufacturing and application processes.[1] The majority of these dyes are hazardous and may cause cancer, therefore, their remediation from industrial effluents is essential for environmental and public health.[2,3] Photocatalysis has attracted significant attention as an alternative to traditional methodology for environmental remediation, as it has advantages such

[a]*Department of Chemistry, COMSATS University Islamabad, Park Road, 45550, Islamabad, Pakistan. E-mail: Jaweria.ambreen@comsats.edu.pk*

[b]*Isotope Production Division (IPD), Pakistan Institute of Nuclear Science and Technology (PINSTECH), P.O. Box 45650, Nilore, Islamabad, Pakistan*

[c]*Department of Nuclear and Quantum Engineering, Korea Advanced Institute of Science and Technology, Daejeon, South Korea*

[d]*Central Analytical Facility Division (CAFD), Pakistan Institute of Nuclear Science and Technology (PINSTECH), Islamabad, Pakistan*

[e]*Chemistry Division, Pakistan Institute of Nuclear Science and Technology (PINSTECH), Islamabad, Pakistan. E-mail: Saifi.551@gmail.com*

[f]*Photovoltaic Research Department, Korea Institute of Energy Research (KIER), Daejeon, South Korea*

[g]*Department of Biomedical Engineering & Health Sciences, Faculty of Electrical Engineering, Universiti Teknologi Malaysia, 81310 UTM, Johor Bahru, Johor, Malaysia*

[h]*Department of Energy Engineering, Korea Institute of Energy Technology, South Korea. E-mail: jhyun@kentech.ac.kr*

† Electronic supplementary information (ESI) available. See DOI: https://doi.org/10.1039/d5ra00969c

as the ability to reduce energy consumption by utilizing natural sunlight, eco-friendliness, and high efficiency.[4–8]

Many semiconductors, such as Fe_2O_3,[9] SnO_2,[10,11] $BiVO_4$,[12] ZnS,[13] Cu_2O, and g-C_3N_4 [14] have been extensively explored in photocatalysis. Besides the semiconductor photocatalysts mentioned above, TiO_2 has been widely explored for its potential to degrade organic contaminants in aqueous solutions.[15] Although TiO_2 is a good photocatalytic material, its wide bandgap of 3.2 eV limits its ability to harness solar energy, as it primarily absorbs UV light below 400 nm. Using TiO_2, only a small portion of incident solar light, falling mainly in the UV region, can be harnessed for targeted chemical reactions. Therefore, visible light-driven photocatalysts with narrow bandgap, or wide bandgap semiconductors coupled with narrow bandgap semiconductors, are preferred as they can utilize a wider spectrum of sunlight.[15]

Graphite carbon nitride, g-C_3N_4 (GCN), is currently being explored for different photocatalytic reactions such as H_2 production, reduction of hexavalent chromium, CO_2 photoreduction, and pollutant degradation.[16,17] GCN is composed of stacked layers of the two-dimensional conjugated framework of s-triazine and has a bandgap of ~2.7 eV.[18] Researchers are drawn towards its exceptional characteristics, such as high thermal, chemical, and mechanical durability, favorable optoelectronic properties, and ecologically benign nature.[19–21] However, pristine GCN has some drawbacks like partial absorption of visible light due to its wide bandgap and fast charge carriers' recombination, which limits its photocatalytic activity.[18]

To improve the photocatalytic performance of the pristine GCN, many efforts have been undertaken, including doping with heteroatoms and metals, construction of the mesoporous structure, copolymerization with organic molecules, and coupling with other semiconductors.[22–25] The construction of its composite with other semiconductors holds great potential to improve its photocatalytic efficiency.[26] A heterojunction is preferably created with a comparatively narrower bandgap material to overcome these drawbacks and enhance GCN's photocatalytic activity. The approach to form a composite with good interfacial contact between two semiconductors with well-matched electronic band structures not only widens the harnessable solar spectrum but also allows efficient charge transfer, which suppresses the recombination of photogenerated electrons and holes.[27] The development of direct Z-scheme photocatalysts has received a lot of interest lately because of their ability to effectively separate photogenerated electron–hole pairs spatially and maximize the photocatalytic system's ability for reduction and oxidation reactions.[28] Yu *et al.* (2013) introduced the idea of a direct Z-scheme photocatalyst to explain strong photocatalytic formaldehyde (HCHO) degradation using TiO_2/GCN composite.[29]

A wide variety of binary heterojunction composites have been made between Ag_3PO_4,[30] Bi_2MoO_6,[31] BiOBr,[32] $NiTiO_3$,[33] ZnO,[34] MnO_2,[35] *etc.* and GCN. Pham and Shin (2018) reported $NiTiO_3$/GCN composite as an excellent photocatalyst for photocatalytic CO_2 reduction.[33] Pradhan *et al.* (2021) communicated MnO_2 modified exfoliated porous GCN nanosheet for enhanced photocatalytic oxidation efficiency of aromatic alcohols.[18] Rashidizadeh *et al.* (2020) described a GCN/$CuWO_4$ nanocomposite for the degradation of methylene blue.[26] Vidyasagar *et al.* (2018) demonstrated (Ag/AgO) loaded GCN for degradation of acidic dyes and bacterial inactivation.[36] The photocatalytic performance has been further improved by employing ternary composite materials.[37] Liu *et al.* (2018) prepared a ternary composite GCN/Ag_3PO_4/Ag_2MoO_4 for producing oxygen from water splitting.[38] Similarly, Tang *et al.* (2020) prepared a ternary composite AgI/Ag_3PO_4/g-C_3N_4 for the degradation of rhodamine B (RhB) under visible light irradiation.[39]

Bismuth subcarbonate ($Bi_2O_2CO_3$) has garnered immense interest due to its chemical stability, non-toxicity, affordability, and environmental friendliness.[40] $Bi_2O_2CO_3$, existing in the sillén phase, has intergrown $(Bi_2O_2)^{2+}$ and $(CO_3)^{2-}$ layers with the orthogonal plane of $(CO_3)^{2-}$ groups.[41] The conduction band of GCN is more negative compared with $Bi_2O_2CO_3$, while the valence band of $Bi_2O_2CO_3$ is more positive relative to GCN.[42,43] Making a composite of $Bi_2O_2CO_3$ with GCN, therefore, is anticipated to improve photocatalytic performance by reducing charge carriers' recombination. However, the visible light absorption of GCN-$Bi_2O_2CO_3$ composite is expected to remain limited as both $Bi_2O_2CO_3$ and GCN have a wide bandgap of 2.41 [44] and 2.70 eV,[45] respectively. To improve visible light absorption and thereby enhance photocatalytic activity, making a mixed phase of $Bi_2O_2CO_3$ with Bi_4O_7, which has a narrow bandgap of 1.89 eV [46] and coupling it with GCN can be effective. This novel approach of making a composite of mixed-phase $Bi_2O_2CO_3$–Bi_4O_7 with GCN will bring the advantage of enhanced photocatalytic activity due to extended absorption of the incident spectrum and increased availability of photo-generated carriers.

In this paper, we report the preparation of ternary composite, g-C_3N_4/$Bi_2O_2CO_3$–Bi_4O_7, photocatalysts with varying weight percentages of $Bi_2O_2CO_3$–Bi_4O_7. The photocatalytic activities of g-C_3N_4/$Bi_2O_2CO_3$–Bi_4O_7 composites are evaluated against RhB degradation and the photoreduction of Cr(VI) under visible light irradiation. The composite sample, having 24 wt% $Bi_2O_2CO_3$–Bi_4O_7, *i.e.*, optimal loading, demonstrated 92.3% of RhB degradation in just 25 min under visible light irradiation. The degradation performance of this composite is considerably better compared with both GCN (73.4%) and $Bi_2O_2CO_3$–Bi_4O_7 (9.4%).

2. Experimentation

2.1 Synthesis of g-C_3N_4

The GCN is synthesized by the thermal polycondensation of urea in a muffle furnace.[47] Briefly, 10 g of urea is placed in a semi-closed alumina crucible with a cover in a muffle furnace and heated to 550 °C for 6 h. Afterward, the alumina crucible is allowed to cool down to room temperature naturally, and the resulting yellow product is collected and ground into powder for further use.

2.2 Preparation of $Bi_2O_2CO_3$–Bi_4O_7 and its composite with GCN

Typically, 0.56 g of $NaBiO_3 \cdot 2H_2O$ is dispersed in 60 mL of water. In the next step, $NaHCO_3$ (1.45 g) is added to the above solution,

stirred for an additional 5 min, and then transferred into a 100 mL Teflon-lined stainless autoclave. The autoclave reactor is heated in an oven at 160 °C for 6 h. After the reaction completion, the $Bi_2O_2CO_3$–Bi_4O_7 (BO) powder is collected by centrifugation, washed with deionized water, and dried at 60 °C for 24 h. To prepare g-C_3N_4/$Bi_2O_2CO_3$–Bi_4O_7 composites, a simple calcination process is adopted. The required amounts of both GCN and BO are dispersed in 60 mL of ethanol using ultrasonication for 90 min. Afterwards, to remove the ethanol, the mixtures are dried at 60 °C for 6 h. To ensure the formation of a composite, the resulting mixture is first ground in a mortar and pestle and then placed in a covered alumina crucible. This mixture is heated for 3 h at 250 °C in a muffle furnace. In the composites, the amounts of BO in GCN are varied from 0 to 30 wt%. In particular, composites with 10, 17, 24, and 30 wt% are prepared and referred to as CN/BO-10, CN/BO-17, CN/BO-24, and CN/BO-30, respectively. The same process conditions are applied to obtain pristine BO.

2.3 Photocatalytic activity assessment

The photocatalytic performance of the six samples, including GCN, BO, and four composite samples, is examined by the degradation of RhB dye under illumination of only visible light. In each photocatalytic experiment, 20 mg of catalyst is added to a 100 mL solution of 10 ppm dye in a Pyrex glass vessel. The solution is stirred for 30 min in the dark before being exposed to a 300 W xenon lamp with a cut-off filter, providing light between 400 to 780 nm, to achieve adsorption and desorption equilibrium between an organic dye and a photocatalyst. Once the irradiation is started, 3 mL of the sample is continuously collected after every 5 min until the degradation is completed. The catalyst is removed from collected liquid samples through centrifugation before analysis by UV-vis spectrophotometry. To quantify RhB dye concentration as a function of time, absorbance is taken at a wavelength of 552 nm; a gradual change in the solution's color is also seen during dye degradation.

2.4 Photocatalytic testing of Cr(VI) reduction

The prepared catalysts, GCN, BO, and CN/BO-24 (*i.e.* composite with optimal loading of BO), are also tested for their activity to photo-reduce Cr(VI) to Cr(III) under visible light irradiation. In a typical Cr(VI) photocatalytic reduction experiment, after dispersing 0.05 g of CN/BO-24 in a 20 ppm Cr(VI) solution, 0.03 mL of 1.02 M H_2SO_4 solution is added. After 30 min of magnetic stirring in the dark, the mixture reaches absorption–desorption equilibrium. Subsequently, the mixed solution is exposed to visible light using a 300 W xenon lamp while using a cut-off filter providing light in the visible region. A 2 mL portion of the reaction solution is regularly collected throughout the photoreduction process. The collected samples are centrifuged in the next step to remove the solid catalyst. To extract 1 mL of the top clear solution from the centrifuge tube, 2 mL of 0.1 M H_2SO_4 and 0.2 mL of 0.10 M diphenylcarbazide are added to it. The UV-vis absorption spectrum of the reaction solution is acquired by using a spectrophotometer. The change in absorbance at a wavelength of 542 nm allows the determination of the Cr(VI) concentration.[48] The following equation is used to determine the percentage photocatalytic Cr(VI) reduction efficiency, $\eta\,(\%) = (1 - C/C_0) \times 100$, where C_0 is the initial concentration and C is the residual Cr(VI) concentration at time t of the photocatalysis experiment.

2.5 Characterization details

The morphology of the materials is measured by a scanning electron microscope, TESCAN MAIA3 Triglav™. The structural characteristics of the samples are examined using an X-ray diffractometer (XRD), EQUINOX 3000, using Cu Kα radiation (wavelength, $\lambda = 1.5406$ Å). Fourier-transform infrared (FTIR) spectra are recorded by NICOLET iS FTIR in a frequency range of 4000–400 cm^{-1}. The photoluminescence (PL) spectra are collected on a Hitachi luminescence spectrophotometer (F-4500), using a He–Ne laser (excitation at 325 nm) as a light source. The CHNS-O analysis is performed by a FLASH 2000 Organic Element Analyzer. Thermogravimetric analysis (TGA) is used to perform thermal analysis of the GCN at a rate of 10 °C min^{-1} by TA Instruments Pyris 1 diamond Q5000IR, New Castle, WA, USA. The UV-vis spectra of degradation of RhB and photoreduction of Cr(VI) are monitored on a Hitachi U-2900 spectrometer and using an HXUV300-T3 (CEA ULIGHT, CHINA) UV lamp for photoreduction experiments. Brunauer–Emmett–Teller (BET) surface area analysis is performed on Micromeritics 3Flex (Version 5.01) analyzer. The samples are degassed for 12 h before analysis and later analyzed using N_2 adsorption at −195.8 °C. The OER experiments are performed with a CorrTest CS2350 electrochemical workstation. The electrochemical characterization details are further described in the ESI.†

3. Results and discussion

3.1 Characterization of the sample

In this study, a total of six samples, including two control samples, *i.e.* GCN and BO, and four GCN-based composites, *i.e.* CN/BO-10, CN/BO-17, CN/BO-24, and CN/BO-30, are prepared. To assess the morphology of pristine, GCN, BO, and GCN-based composites with different weight ratios of BO, SEM analysis is performed. SEM image of GCN in Fig. 1(a) shows that it is composed of agglomerated nanosheets. Sun *et al.* (2017) also reported similar morphology for GCN, where solid agglomerates in the micrometer size range were composed of nanosheets.[46] In Fig. 1(b), pure BO possesses, in general, rod-like morphology in addition to irregularly shaped particles. The SEM images of different GCN-based composites in Fig. 1(c–f) clearly show the dispersion of BO in the GCN nanosheet matrix. In all SEM images of composites, BO rods or other irregularly shaped particles can be clearly seen. The close interaction between GCN and BO may promote the interfacial transport of photo-generated carriers and, thereby, improve the photocatalytic performance.

Fig. 2 shows the XRD diffractograms of as-synthesized GCN, BO, and CN/BO composites with 10, 17, 24, and 30 wt% of BO. XRD pattern of GCN, as can be seen in Fig. 2, clearly shows two

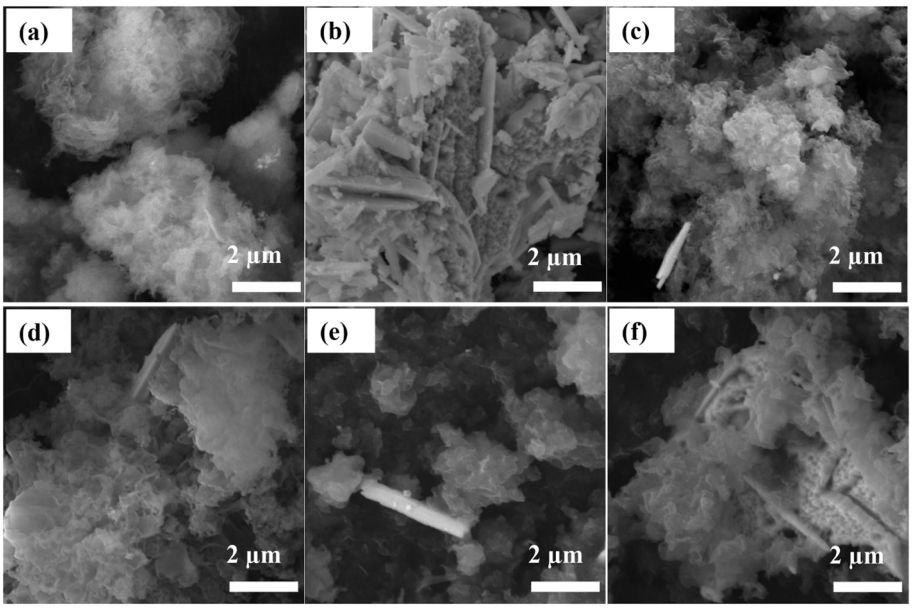

Fig. 1 SEM images of (a) GCN, (b) BO, (c) CN/BO-10, (d) CN/BO-17, (e) CN/BO-24, and (f) CN/BO-30.

distinctive diffraction peaks at 13.1 and 27.4° that can be indexed to the (002) and (100) crystal planes, respectively (PDF card no. 087-1526). The XRD analysis of BO indicates its successful synthesis, *i.e.* mixture of $Bi_2O_2CO_3$ and Bi_4O_7. The composite or mixed phase of these materials as a photocatalyst has been reported to perform better compared with the phase-pure $Bi_2O_2CO_3$ [45] and Bi_4O_7.[15] In $Bi_2O_2CO_3$, peaks at 12.9, 23.9, 26.0, 30.2, 32.7, 39.5, 42.2, 46.9, 52.2, 53.4, and 56.8° correspond to (002), (011), (004), (013), (110), (006), (114), (020), (116), (121), and (123) planes, respectively, of PDF card no. 00-041-1488. In addition, other peaks at 27.6, 28.3, and 31.3° corresponding to (2−2−2), (22−2), and (400) planes, respectively, are also observed. These characteristic peaks belong to Bi_4O_7 with PDF card no. 00-47-1058. In BO, the majority of observed peaks belong to $Bi_2O_2CO_3$, whereas only a few peaks are found for Bi_4O_7. Liu *et al.* (2021) reported that high-temperature processing of $Bi_2O_2CO_3$ converts it into the corresponding oxide phases.[15] In this study, the formation of $Bi_2O_2CO_3$–Bi_4O_7 mixed phase can be attributed to high temperature and pressure conditions during hydrothermal reaction and annealing at 250 °C during the composite preparation step. For fair comparison of BO with composite samples, BO after its synthesis by the hydrothermal method is also subjected to annealing at 250 °C. Because of the overlapping of the diffraction peaks for Bi_4O_7 (27.6°) and g-C_3N_4 (27.4°), it is difficult to distinguish their individual peak. Ge *et al.* (2011) have also observed a similar overlapping of diffraction peaks in g-C_3N_4/Bi_2WO_6.[49] Most of the peaks correspond to $Bi_2O_2CO_3$ in all the composites, indicating that both Bi_4O_7 and $Bi_2O_2CO_3$ phases are present. Therefore, it can be concluded that the composites contain GCN, Bi_4O_7, and $Bi_2O_2CO_3$.

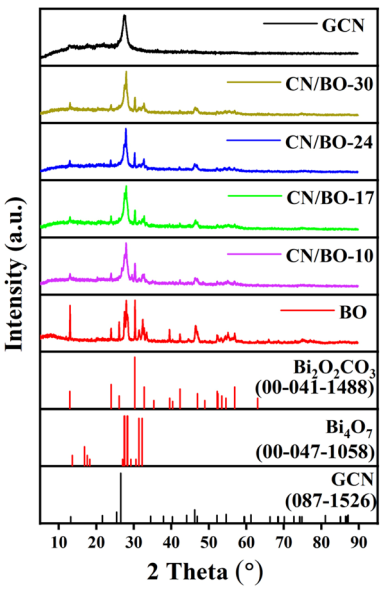

Fig. 2 XRD patterns of pristine GCN, BO, CN/BO-10, CN/BO-17, CN/BO-24, and CN/BO-30. The standard diffraction lines imported from corresponding PDF card numbers of GCN, Bi_4O_7, and $Bi_2O_2CO_3$ are also shown at the bottom.

FTIR analysis is performed to examine different vibration modes in pristine GCN, BO, and the prepared CN/BO composites. The resulting FTIR spectra are displayed in Fig. 3. Pure GCN exhibits its distinctive vibration peaks at wave numbers of 808, 1230, 1313, 1537, 1632, and 3185 cm^{-1}, which is in accordance with results reported by Tian *et al.* (2014).[45] The wide band at 3185 cm^{-1} appears to be related to the –OH groups, most likely due to adsorbed water molecules and the stretcting vibrations of –NH groups.[50,51] The triazine units yielded a peak at 808 cm^{-1}, whereas the stretching vibration of the C–N heterocyclic is reflected between 1233 to 1537 cm^{-1}. The C–N and C=N stretching modes are represented by the peaks at

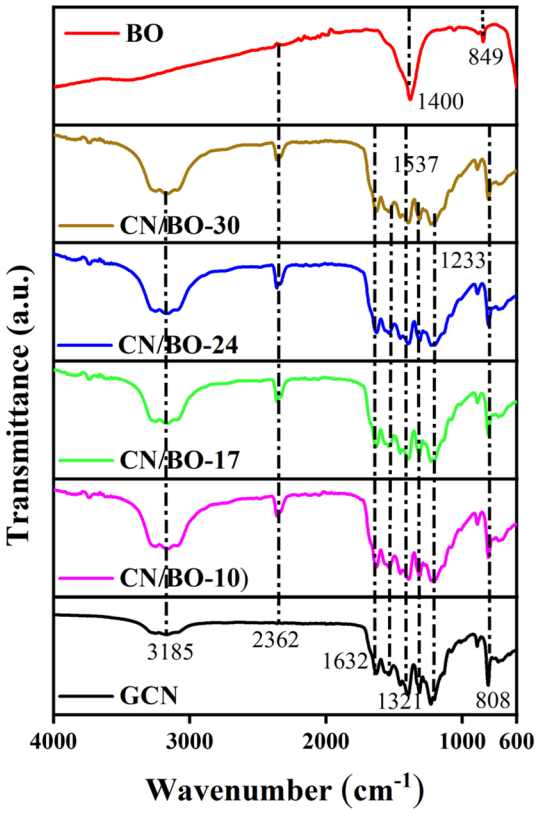

Fig. 3 FTIR patterns of pristine GCN and BO, as well as composites CN/BO-10, CN/BO-17, CN/BO-24, and CN/BO-30.

1313 and 1632 cm^{-1}, respectively.[51] Regarding the BO, the stretching vibrations of the Bi–O–Bi in the compound are responsible for a peak at about 849 cm^{-1}, whereas the stretching vibrations of C–O and C=O are manifested in a form of broad peaks at around 1400 cm^{-1}.[15]

In the case of CN/BO composite samples (CN/BO-10, CN/BO-17, CN/BO-24, and CN/BO-30), the FTIR spectra display a combination of vibrational features from both GCN and BO components, confirming successful composite formation. All CN/BO composites exhibit peaks in the region of 1233–1537 cm^{-1}, indicating the retention of C–N stretching modes, and the peak around 1632 cm^{-1} denoting the C=N stretching. A difference that is visible in composite samples compared with the pristine GCN and BO is the emergence of a peak at 2362 cm^{-1} which arises from the stretching vibration of surface-adsorbed CO_2.[52] The CO_2 in composite samples comes from the decomposition of CO_3 in $Bi_2O_2CO_3$, which gets adsorbed in high surface area GCN. A high surface area of GCN is confirmed from the BET analysis which will be discussed in Section 3.2. A similar vibration peak originating from CO_2 does not emerge in BO, most probably because of its small surface area. To confirm the successful composite formation, selected regions of FTIR patterns of only GCN and CN/BO-24 are shown in Fig. S1.† On having a close look at the 1233–1537 cm^{-1} region in Fig. S1(a),† it is observed that peaks related to s-trizine system are red-shifted. For instance, 1205, 1230, 1397, 1455, and 1537 cm^{-1} are shifted to lower wavenumbers. Such a red shift in FTIR peaks of GCN in the composite samples originates from the electronic interaction between the two constituents of the composite. The nitrogen sites in GCN can interact with Bi cations in BO, which act as a Lewis acid, while nitrogen functions as a Lewis base. The other possible interaction that in parallel can lead to such a red shift is the hydrogen bonding between amines in GCN and CO_3^{-2} functionalities in the $Bi_2O_2CO_3$. These interactions result in the weakening of C–N bonds in GCN. Fig. S1(b)† shows that another peak at 808 cm^{-1} in the composite (*i.e.* CN/BO-24) relating to GCN triazine units bending vibration is also red-shifted.[53] These spectral changes collectively confirm the successful formation of a well-integrated CN/BO composite with strong interfacial interactions and altered vibrational properties.

To assess the separation efficiency and the degree of recombination of the photogenerated electrons and holes in GCN and CN/BO composite, photoluminescence (PL) analysis is performed. The PL emission gets intense as the photogenerated carriers' recombination efficiency in a semiconductor increases.[45] Therefore, the photocatalytic material's performance will be compromised due to the lower availability of carriers. The PL spectra of the pristine GCN as well as composite samples (*i.e.* CN/BO-10, CN/BO-17, CN/BO-24, and CN/BO-30) are shown in Fig. 4. It can be observed in Fig. 4 that GCN has an emission peak at a wavelength (λ) of 456 nm. This emission wavelength corresponds to a bandgap (E_g) of 2.72 eV, which is in accordance with the literature.[45] On adding BO to GCN for up to 24 wt%, the PL emission intensity gradually decreases, which can be attributed to the reduced recombination of photogenerated carriers in composite samples. Tian *et al.* (2015) also reported a decrease in the intensity of PL spectra by $BiVO_4$/g-C_3N_4 composite, which was attributed to reduced charge carrier recombination as compared to GCN.[54] On further increasing the BO content in GCN up to 30 wt%, PL emission again gets intense, and the peak intensity becomes almost equivalent to that of GCN. This reversal of trend in the PL emission intensity suggests that, in terms of carriers' lifetime, the best composite sample is CN/BO-24, and the approach to couple GCN with BO

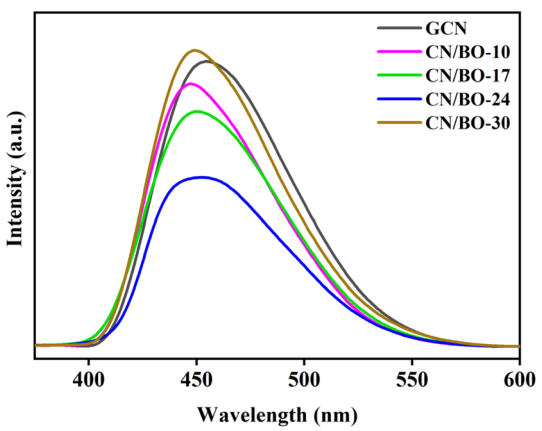

Fig. 4 Photoluminescence spectra of pristine GCN, BO, CN/BO-10, CN/BO-17, CN/BO-24, and CN/BO-30 composites taken with a He–Ne laser with excitation wavelength 325 nm.

seems to bring positive implications toward photocatalytic performance. The results on the photocatalytic performance as a function of BO loading in CN/BO composite will be presented in the proceeding section.

The elemental composition analysis of GCN, BO, CN/BO-10, CN/BO-17, CN/BO-24, and CN/BO-30 is also performed to check if the GCN retains its structure in composite samples. GCN is primarily composed of carbon and nitrogen, forming a polymeric structure of triazine units. The N/C molar ratio in the prepared GCN is found to be 1.54, which is higher than what one could expect in C_3N_4, *i.e.*, 1.33. Nithya and Ayyappan (2020) also reported an N/C molar ratio of 1.47 for GCN.[55] In pristine BO, 0.94% of C is detected, suggesting the presence of $Bi_2O_2CO_3$ in addition to Bi_4O_7. This once again validates the results of the XRD analysis. Additionally, it also has 13.69% of O content. In the composite samples, the N/C ranges from 1.52 to 1.54 and shows only a small variation between samples. This implies that GCN stoichiometry has not changed considerably during the composite preparation step. Further, the relatively higher percentage content of C and N in the composite suggests that GCN acted as a matrix in the composite samples.

The thermal stability of GCN is assessed by thermogravimetric analysis (TGA), as shown in Fig. S2.† The TGA analysis indicated that GCN remains stable up to 500 °C. Differential thermogravimetric analysis (not shown) revealed that GCN showed a peak at 638 °C, which can be attributed to its degradation. Wang *et al.* (2012) also reported a peak at 630 °C in GCN.[56] This indicates that GCN retains its structure during the preparation of composite samples through the annealing process carried out at 250 °C, which is also corroborated by the CHNS-O analysis discussed above.

3.2 Photocatalytic activity

The photocatalytic activities of the prepared samples are evaluated against organic dye, RhB, under a 300 W Xe lamp equipped with a filter that only allows light with wavelengths 400–780 nm to pass through. Fig. 5(a) shows the degradation results of RhB (10 ppm) over pristine BO and pristine GCN along with its composites with BO, *i.e.*, CN/BO-10, CN/BO-17, CN/BO-24, and CN/BO-30. It can be observed that pure BO exhibits poor activity for RhB, with only 9.4% after 45 min of irradiation. The 90.6% degradation of RhB is achieved in 45 min of irradiation when GCN is used as the photocatalyst. The CN/BO-10 and CN/BO-17 exhibit degradation of 94.5% and 95.3%, respectively, in 45 min, which is slightly better compared with GCN. Their degradation performance *versus* time is overall higher relative to GCN as well. This increase in the performance shows a positive impact of BO loading on the GCN photocatalytic performance. On raising the BO loading to 24% (CN/BO-24), the photocatalytic activity is considerably increased, with 98.3% degradation of dye after 45 min. The performance of CN/BO-30, on the other hand, deteriorates, as the degradation of only 89.6% is achieved in 45 min. The performance of CN/BO-30 is even inferior to GCN, CN/BO-10, and CN/BO-17. The percentage degradation values of RhB within 25 min by GCN, BO, CN/BO-10, CN/BO-17, CN/BO-24, and CN/BO-30 are 73.4, 9.4, 79.4, 82.8, 92.3, and 65.5%, respectively, as shown in Fig. 5(b). This indicates that the CN/BO-24 composite performed better in comparison to pristine GCN, BO, and other composites. The UV-vis absorption curves of RhB solution, while using CN/BO-24 catalyst, are recorded at different time intervals of photo-irradiation. As shown in Fig. 5(c), it can be concluded that RhB is almost degraded in 25 min. In terms of degradation performance, CN/BO-24 performs best as it has the optimal loading of BO. The activities in a composite photocatalytic system are greatly influenced by the components constituting the photocatalyst.

Both improved separation of photogenerated carriers and increased visible light absorption seem responsible for boosting the photocatalytic activity of CN/BO-24. Therefore, the ideal concentration of BO in GCN for a composite photocatalyst is 24%, where the optimum combination for both light absorption and charge transfer is achieved. Increasing the BO loading in GCN to 30% might increase the light absorption, however, the charge transfer and the reaction at the surface of the catalyst will be limited due to the low concentration of GCN and possible aggregation of BO and its low surface area. This may badly impact the photocatalytic performance. In Fig. 5(b), it is evident that the CN/BO-24 composite demonstrates superior degradation performance, achieving almost complete degradation within just 25 min, with a degradation performance of approximately 92.3%. This suggests that the combination of BO and GCN in the CN/BO-24 composite effectively suppresses charge carrier recombination, enhancing its photocatalytic efficiency.

To assess the available surface area (SA) of the prepared photocatalysts, BET analysis of pristine samples, GCN, and BO is performed. This measurement can reveal any existing correlation between the enhanced photocatalytic performance and the SA of the composite. The SA is found to be 38.7835 $m^2\ g^{-1}$ for GCN and 1.4526 $m^2\ g^{-1}$ for BO (data not shown). Following the wt% ratio of the GCN and BO in the best-prepared composite CN/BO-24, the theoretical SA is determined to be 30.1687 $m^2\ g^{-1}$, which is lower compared to the SA of GCN. Although SA can influence the number of active sites available for dye adsorption and degradation, photocatalytic performance is often more strongly governed by charge carrier dynamics, especially in reactions involving visible light-driven processes. The superior activity of the composite, *i.e.* CN/BO-24, can be attributed to enhanced charge separation and reduced recombination rate, which are likely a result of favorable synergistic electronic interactions at the GCN–BO interface. The efficient charge transfer prolongs the lifetime of charge carriers, making them more available for dye degradation. The PL study, as shown in Fig. 4, also indicates the low charge carriers' recombination of the CN/BO-24 composite.

To study the kinetics of the photo-degradation process, data is fitted with a pseudo-first-order kinetics equation, $\ln(C/C_o) = -kt$, where C_0 is the initial concentration, C is the concentration at different time intervals, k is the kinetic constant, and t is the time. The fitted data, shown in Fig. 5(d), indicate that the photo-degradation process of the prepared catalysts follows a pseudo-first-order kinetics. The values of k for the prepared catalysts are

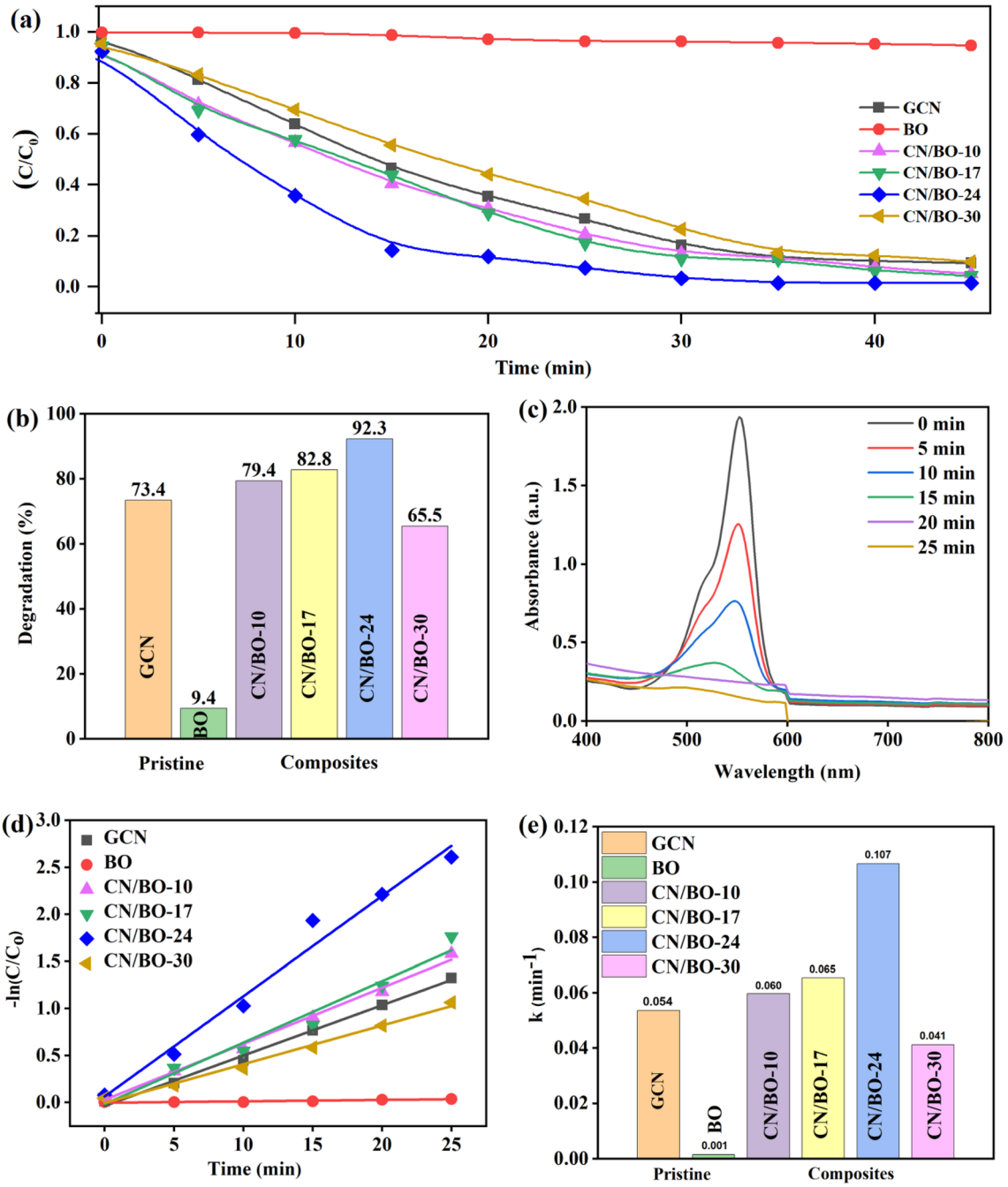

Fig. 5 (a) Photocatalytic degradation of RhB dye as a function of time for up to 45 min, (b) percentage degradation of RhB by GCN, BO, CN/BO-10, CN/BO-17, CN/BO-24, and CN/BO-30 after 25 min, (c) UV-vis absorption curves taken at different time intervals of photo-irradiation for CN/BO-24, (d) $-\ln(C/C_0)$ *versus* time plot obtained against RhB photocatalytic degradations for different samples, and (e) rate constant values obtained for different samples from pseudo-first-order fitting. Photocatalytic reactions are performed under a 300 W Xe lamp having a filter that transmits light in the 400–780 nm range.

presented in Fig. 5(e). The degradation rate constant of GCN and BO for RhB in the degradation process is 0.054 and 0.001 min^{-1}, respectively, again indicating that the photocatalytic efficiency of GCN is better in comparison to BO. The values of k for CN/BO-10, CN/BO-17, CN/BO-24, and CN/BO-30 are 0.060, 0.065, 0.107, and 0.041 min^{-1}, respectively. Fig. 4(d) shows that the kinetic constant k of CN/BO-24 degradation is about 2 and 72 times higher than that of pure GCN and BO, respectively.

An additional crucial factor for the practical use of the produced photocatalyst in environmental applications is its regenerative stability under light irradiation. Fig. 6(a) illustrates the RhB photo-degradation profiles *versus* time with CN/BO-24 composite in the three successive runs. The percentage degradation of RhB in 45 min in the first, second, and third runs is

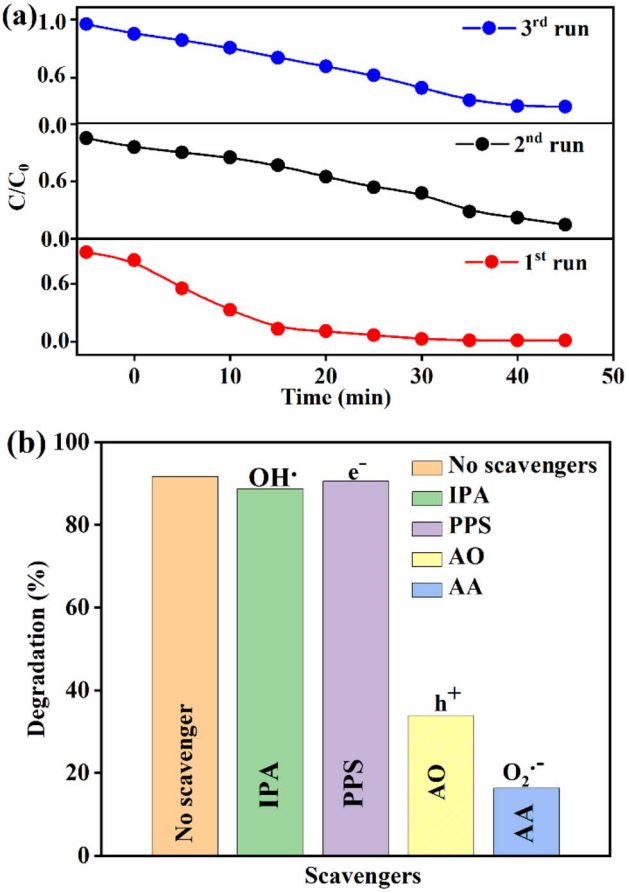

Fig. 6 (a) The photocatalytic degradation of RhB is repeated three times using CN/BO-24 under visible light irradiation. RhB concentration in these experiments is 10 ppm while the catalyst used is 20 mg. (b) Effect of different scavengers, *i.e.* IPA, PPS, AO, and AA, on the percentage photo-degradation of RhB by using CN/BO-24. The amounts of different scavengers, RhB, and catalysts in these degradation experiments are 1 mmol, 10 ppm, and 20 mg, respectively. Each degradation experiment is performed for 25 min.

98.3, 85.8, and 73.0%, respectively, which indicates a slight decrease in repetitive use. To verify any potential phase changes in the catalyst following photocatalytic degradation, XRD analysis is conducted, as shown in Fig. S3.† The results indicate that the catalyst retains the same phase before and after the photocatalytic activity, demonstrating the stability of the prepared photocatalyst.

3.3 Active species trapping experiments

To fully understand the photocatalytic process, active species trapping experiments are carried out by using scavenging agents (1 mmol). Ascorbic acid (AA), ammonium oxalate (AO), potassium persulfate (PPS), and isopropyl alcohol (IPA), to scavenge superoxide radicals ($O_2^{\bullet-}$), holes (h^+), electrons (e^-), and hydroxyl radicals ($^{\bullet}OH$), respectively. Fig. 6(b) displays RhB percentage degradation in the presence of different scavengers. The addition of IPA results in a modest reduction in the rate of RhB degradation, suggesting that $^{\bullet}OH$ is not essential for the

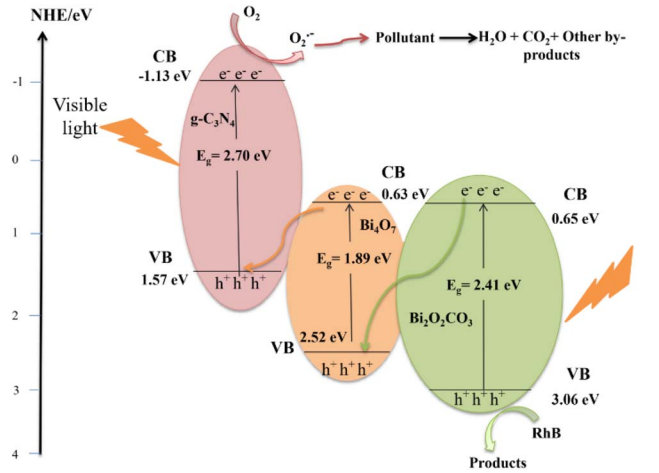

Fig. 7 Proposed photocatalytic degradation mechanism of organic contaminants (RhB) in the presence of CN/BO composite. The CB and VB potentials of $Bi_2O_2CO_3$, GCN, and Bi_4O_7 are obtained from previous studies.[44–46]

photocatalytic degradation process. Nevertheless, the RhB degradation is considerably affected by the addition of AA and AO, indicating that h^+ and $O_2^{\bullet-}$ are the primary species involved in the photocatalytic activity.

Ultimately, by combining the previously determined bandgap values, as well as the conduction band (CB) and valence band (VB) position of pure components, an energy band diagram of the potential ternary composite photocatalytic process can be anticipated. Fig. 7 shows the potential photodegradation schematic mechanism in a ternary heterojunction structure. Under visible light irradiation, GCN, Bi_4O_7, and $Bi_2O_2CO_3$ are all excited, leading to the generation of electron–hole pairs. However, the extent of photo-generation of carriers is controlled by the bandgap value, which is the lowest in Bi_4O_7. The electrons in the CB of $Bi_2O_2CO_3$ (0.65 eV)[44] recombine with holes in the VB of Bi_4O_7 (2.52 eV).[46] Simultaneously, electrons in CB of Bi_4O_7 (0.63 eV) recombine with holes in the VB of GCN (1.57 eV).[45] As a result, electrons accumulate in the CB of GCN (−1.13 eV), which has a more negative edge, while holes build up in the VB of $Bi_2O_2CO_3$ (3.06 eV), which has a more positive VB edge. Since the CB edge of GCN is more negative, the photogenerated electrons that accumulate in the CB of GCN have strong reducing power and react with O_2 to form $O_2^{\bullet-}$ radicals. These $O_2^{\bullet-}$ radicals contribute to the decomposition of RhB. Meanwhile, the holes that remain in VB of $Bi_2O_2CO_3$ exhibit strong oxidizing ability and directly react to the RhB molecules, breaking them down into products.

Table 1 compares the effectiveness of GCN combined with other photocatalysts in the degradation of RhB dye. The photocatalysts are mentioned along with their RhB degradation percentage, the time required, and the active quenching agents. It is evident from Table 1 that the ternary g-C_3N_4/$Bi_2O_2CO_3$–Bi_4O_7 composite exhibits better degradation of RhB within a short time, showing a notable improvement in photocatalytic efficiency compared with other reported binary composites.

Table 1 A summary of the photocatalytic degradation performance of different composite photocatalysts that include GCN for the degradation of RhB dye

Year	Composite photocatalyst	% Degradation of RhB	Time	Quenching agents	References
2014	BiOCl/GCN	99	60 min	h^+, $O_2^{\cdot-}$	57
2015	$BiVO_4$/GCN	85	5 h	$^{\cdot}OH$, $O_2^{\cdot-}$	54
2015	SnO_2/GCN	98.7	100 min	h^+, $O_2^{\cdot-}$	58
2017	WO_3/GCN	~100	2 h	$^{\cdot}OH$, $O_2^{\cdot-}$	59
2017	GCN/TiO_2	95.2	80 min	h^+, $O_2^{\cdot-}$	60
2024	GCN/$Bi_2O_2CO_3$–Bi_4O_7	98.3	45 min	h^+, $O_2^{\cdot-}$	This study

The release of chromium (Cr) from industrial effluents into the environment is a cause of pollution.[61] Cr in the environment exists in two main oxidation states, Cr(VI) and Cr(III). Cr(VI) is carcinogenic, mutagenic, and can cause a variety of health issues, therefore, its release in the environment has to be controlled.[62] In contrast, the toxicity of Cr(III) is relatively low. To limit the adverse effect of Cr on the environment, Cr(VI) needs to be reduced to Cr(III).[63] In this study, the prepared catalysts are also checked for their efficacy against the photoreduction of Cr(VI).

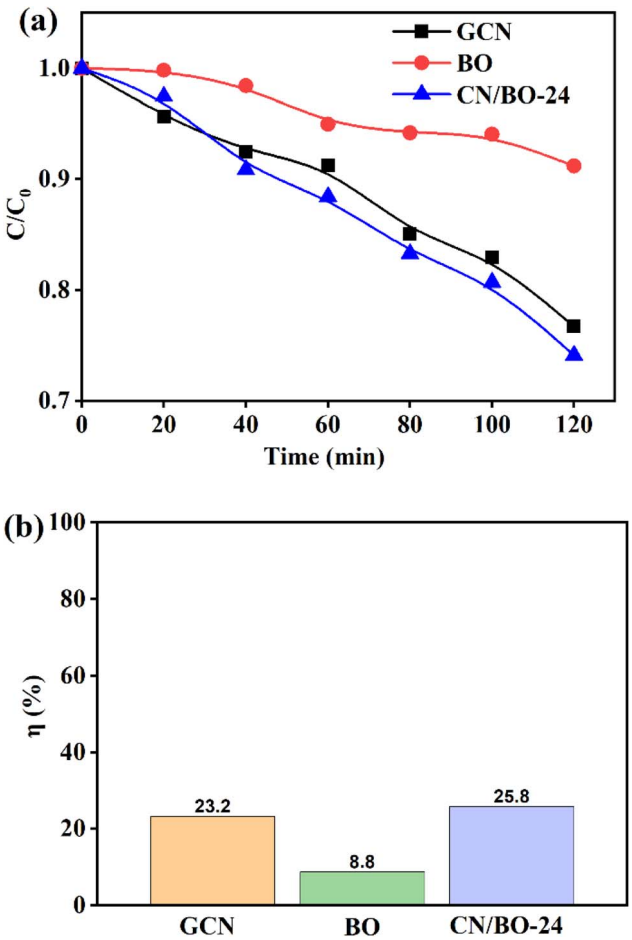

Fig. 8 (a) Photocatalytic reduction of Cr(VI) to Cr(III) *versus* time and (b) percentage photocatalytic Cr(VI) reduction efficiency of GCN, BO, and CN/BO-24 after 120 min of visible light irradiation.

Fig. 8(b) shows the photoreduction performance *versus* time as well as photoreduction efficiency (η) of Cr(VI) using GCN, BO, and CN/BO-24 after 120 min of visible light irradiation. It is evident from Fig. 8(a) that the reduction efficiency in the case of BO is comparatively poor, whereas GCN and CN/BO-24 exhibited relatively better performance. Fig. 8(b) further shows that after 120 min, the η values for GCN, BO, and CN/BO-24 are 23.2, 8.8, and 25.8%, respectively. The η value is found to be the highest for CN/BO-24. The reduction mechanism is closely linked to electron–hole separation efficiency facilitated by the ternary composite of GCN, Bi_4O_7, and $Bi_2O_2CO_3$. A similar trend is observed in both Cr(VI) photoreduction and RhB degradation studies. The photogenerated electrons in the CB of GCN are vital in Cr(VI) reduction, as they provide the necessary reducing power to convert toxic Cr(VI) to Cr(III).

The performance of the oxygen evolution reaction (OER) is also evaluated by using GCN, BO, and CN/BO-24, as shown in Fig. S4.† From the results, it can be concluded that GCN displays better electrochemical performance for OER, while the CN/BO-24 composite exhibits the best photocatalytic performance.

4. Conclusion

Photocatalytic materials play a crucial role in environmental remediation by reducing energy consumption through utilizing naturally available sunlight. Graphitic carbon nitride, g-C_3N_4 (GCN), is a promising photocatalytic material; however, its limited absorption in the visible light spectrum hinders its overall efficiency. In this study, GCN composites are prepared with $Bi_2O_2CO_3$–Bi_4O_7 (BO) to enhance their photocatalytic activity. The amount of BO in composites is varied; the optimal loading for photocatalytic degradation of rhodamine B (RhB) is found to be 24 wt%. The CN/BO-24 (*i.e.*, composite having 24 wt% of BO) demonstrated considerably higher activity in comparison to the pristine GCN and BO under visible light irradiation. The RhB dye degradation is 92.3% in 25 min for CN/BO-24, compared with 73.4% for GCN and 9.4% for BO. The pseudo-first-order degradation rate constant, k, of CN/BO-24 is about 2 and 72 times higher in comparison to the pure GCN and BO, respectively. Additionally, the photoreduction evaluation of Cr(VI) demonstrates improved reduction efficiency (η) of 25.8% for CN/BO-24, compared to 23.2% for GCN and 8.8% for BO. Active species trapping experiments reveal

that peroxide radicals ($O_2^{\bullet -}$) and holes (h^+) are the key active species involved in the photocatalytic degradation of RhB. A comparison with existing literature suggests that the GCN-based photocatalyst developed in this study outperforms previously reported similar catalysts.

Data availability

Data can be provided upon request.

Conflicts of interest

There are no conflicts to declare.

Acknowledgements

The authors acknowledge the support of the Physics Division, Central Analytical Facility Division, and Chemistry Division at PINSTECH, as well as the National Institute of Laser and Optronics (NILOP), for their support in providing resources and access to various analytical techniques used in this study. The author S. Mehboob hereby acknowledge KIST School Partnership Project.

References

1 E. Forgacs, T. Cserháti and G. Oros, *Environ. Int.*, 2004, **30**, 953–971.
2 S. Parsons, *Advanced Oxidation Processes for Water and Wastewater Treatment*, IWA publishing, 2004.
3 M. Feng, T. Zhou, J. Li, M. Cao, J. Cheng, D. Li, J. Qi and F. You, *Molecules*, 2024, **29**, 5423.
4 Q. Liu, Y. Zhou, J. Kou, X. Chen, Z. Tian, J. Gao, S. Yan and Z. Zou, *J. Am. Chem. Soc.*, 2010, **132**, 14385–14387.
5 Z. Wang, Y. Huang, W. Ho, J. Cao, Z. Shen and S. C. Lee, *Appl. Catal., B*, 2016, **199**, 123–133.
6 D. Spasiano, R. Marotta, S. Malato, P. Fernandez-Ibanez and I. Di Somma, *Appl. Catal., B*, 2015, **170**, 90–123.
7 S. Wang, J. Lin and X. Wang, *Phys. Chem. Chem. Phys.*, 2014, **16**, 14656–14660.
8 Y. Zhao, Z. Guo, Y. Wang, M. Birkett, X. Xiang, C. Zhang, Y. Jin, G. Che, H. Wang and C. Liu, *J. Environ. Chem. Eng.*, 2024, **12**, 112974.
9 M. Mishra and D.-M. Chun, *Appl. Catal., A*, 2015, **498**, 126–141.
10 P. Luque, O. Nava, C. Soto-Robles, M. Chinchillas-Chinchillas, H. Garrafa-Galvez, Y. Baez-Lopez, K. Valdez-Núñez, A. Vilchis-Nestor and A. Castro-Beltrán, *Optik*, 2020, **206**, 164299.
11 M. Zahra, M. Saifullah, A. Majeed, S. Hassan, K. Shehzad, M. A. R. Anjum, S. Mehboob, M. Rehan, M. Gul and J. Ambreen, *J. Mater. Chem. C*, 2024, **12**, 14376–14386.
12 H. Duan, H. Wu, H. Zhong, X. Wang, W. Wan, D. Li, G. Cai, C. Jiang and F. Ren, *J. Phys. Chem. C*, 2022, **126**, 7688–7695.
13 W. Wang, B. Li, H.-J. Yang, Y. Liu, L. Gurusamy, L. Karuppasamy and J. J. Wu, *Nanomaterials*, 2021, **11**, 3380.
14 Q. Shi, X. Zhang, X. Liu, L. Xu, B. Liu, J. Zhang, H. Xu, Z. Han and G. Li, *Carbon*, 2022, **196**, 401–409.
15 X. Liu, Q. Fan, F. Li, L. Wei and C. Yu, *J. Nanopart. Res.*, 2021, **23**, 1–16.
16 Q. Wang, Y. Li, F. Huang, S. Song, G. Ai, X. Xin, B. Zhao, Y. Zheng and Z. Zhang, *Molecules*, 2023, **28**, 432.
17 Z. Xie, Q. Gao, X. Shang, X. Fu, J. Yang, Y. Yan and Q. Li, *Green Carbon*, 2024, **2**, 366–382.
18 M. R. Pradhan, D. Rath, R. Sethi, B. B. Nanda and B. Nanda, *Inorg. Chem. Commun.*, 2021, **130**, 108717.
19 M. Pradhan, S. Panda and B. Nanda, *Biointerface Res. Appl. Chem.*, 2020, **10**, 5021–5027.
20 S. Zhang, P. Gu, R. Ma, C. Luo, T. Wen, G. Zhao, W. Cheng and X. Wang, *Catal. Today*, 2019, **335**, 65–77.
21 G. Mamba and A. Mishra, *Appl. Catal., B*, 2016, **198**, 347–377.
22 J. Wu, N. Li, X.-H. Zhang, H.-B. Fang, Y.-Z. Zheng and X. Tao, *Appl. Catal., B*, 2018, **226**, 61–70.
23 Z. Zhao, Y. Dai, J. Lin and G. Wang, *Chem. Mater.*, 2014, **26**, 3151–3161.
24 W. Ho, Z. Zhang, W. Lin, S. Huang, X. Zhang, X. Wang and Y. Huang, *ACS Appl. Mater. Interfaces*, 2015, **7**, 5497–5505.
25 H. Yu, F. Chen, F. Chen and X. Wang, *Appl. Surf. Sci.*, 2015, **358**, 385–392.
26 A. Rashidizadeh, H. Ghafuri and Z. Rezazadeh, *Proceedings*, 2020, **41**, 43.
27 C. Yu, G. Li, S. Kumar, K. Yang and R. Jin, *Adv. Mater.*, 2014, **26**, 892–898.
28 J. Low, C. Jiang, B. Cheng, S. Wageh, A. A. Al-Ghamdi and J. Yu, *Small Methods*, 2017, **1**, 1700080.
29 J. Yu, S. Wang, J. Low and W. Xiao, *Phys. Chem. Chem. Phys.*, 2013, **15**, 16883–16890.
30 M. D. Kumar and R. Padmanaban, *Indian J. Chem. Technol.*, 2022, **28**, 595–603.
31 R. Chen, L. Wang, J. Ding, J. Zhang, H. Wan and G. Guan, *J. Alloys Compd.*, 2023, **960**, 170605.
32 L. Ye, J. Liu, Z. Jiang, T. Peng and L. Zan, *Appl. Catal., B*, 2013, **142**, 1–7.
33 T.-T. Pham and E. W. Shin, *Langmuir*, 2018, **34**, 13144–13154.
34 R. C. Ngullie, S. O. Alaswad, K. Bhuvaneswari, P. Shanmugam, T. Pazhanivel and P. Arunachalam, *Coatings*, 2020, **10**, 500.
35 P. Xia, B. Zhu, B. Cheng, J. Yu and J. Xu, *ACS Sustain. Chem. Eng.*, 2018, **6**, 965–973.
36 D. Vidyasagar, S. G. Ghugal, A. Kulkarni, P. Mishra, A. G. Shende, S. S. Umare and R. Sasikala, *Appl. Catal., B*, 2018, **221**, 339–348.
37 Y. Guo, Y. Ao, P. Wang and C. Wang, *Appl. Catal., B*, 2019, **254**, 479–490.
38 W. Liu, J. Shen, X. Yang, Q. Liu and H. Tang, *Appl. Surf. Sci.*, 2018, **456**, 369–378.
39 M. Tang, Y. Ao, C. Wang and P. Wang, *Appl. Catal., B*, 2020, **268**, 118395.
40 C. M. Bedoya Hincapie, M. J. Pinzon Cardenas, J. E. Alfonso Orjuela, E. Restrepo Parra and J. J. Olaya Florez, *Dyna*, 2012, **79**, 139–148.
41 Y. Tsunoda, W. Sugimoto and Y. Sugahara, *Chem. Mater.*, 2003, **15**, 632–635.

42 Y. He, J. Cai, L. Zhang, X. Wang, H. Lin, B. Teng, L. Zhao, W. Weng, H. Wan and M. Fan, *Ind. Eng. Chem. Res.*, 2014, **53**, 5905–5915.
43 J. Cao, X. Li, H. Lin, S. Chen and X. Fu, *J. Hazard. Mater.*, 2012, **239**, 316–324.
44 S. Zhong, H. Zhou, M. Shen, Y. Yao and Q. Gao, *J. Alloys Compd.*, 2021, **853**, 157307.
45 N. Tian, H. Huang, Y. Guo, Y. He and Y. Zhang, *Appl. Surf. Sci.*, 2014, **322**, 249–254.
46 M. Sun, Y. Wang, Y. Shao, Y. He, Q. Zeng, H. Liang, T. Yan and B. Du, *J. Colloid Interface Sci.*, 2017, **501**, 123–132.
47 L. T. Hang, N. D. Lai, N. T. Phuong, D. V. Thang, N. M. Hung and N. Van Minh, *Phys. B*, 2018, **532**, 48–53.
48 L. Li, H. Gao, G. Liu, S. Wang, Z. Yi, X. Wu and H. Yang, *Adv. Powder Technol.*, 2022, **33**, 103481.
49 L. Ge, C. Han and J. Liu, *Appl. Catal., B*, 2011, **108**, 100–107.
50 W. Zou, Y. Shao, Y. Pu, Y. Luo, J. Sun, K. Ma, C. Tang, F. Gao and L. Dong, *Appl. Catal., B*, 2017, **218**, 51–59.
51 Y. Zang, L. Li, Y. Zuo, H. Lin, G. Li and X. Guan, *RSC Adv.*, 2013, **3**, 13646–13650.
52 M. O. Yusuf, *Appl. Sci.*, 2023, **13**, 3353.
53 N. A. Nordin, M. A. Mohamed, M. S. Mastuli, S. F. M. Yusoff, T. Sugiura and K. Manseki, *J. Ind. Eng. Chem.*, 2024, **135**, 197–212.
54 N. Tian, H. Huang, Y. He, Y. Guo, T. Zhang and Y. Zhang, *Dalton Trans.*, 2015, **44**, 4297–4307.
55 R. Nithya and S. Ayyappan, *J. Photochem. Photobiol., A*, 2020, **398**, 112591.
56 X. Wang, S. Blechert and M. Antonietti, *ACS Catal.*, 2012, **2**, 1596–1606.
57 Y. Bai, P.-Q. Wang, J.-Y. Liu and X.-J. Liu, *RSC Adv.*, 2014, **4**, 19456–19461.
58 X. Chen, B. Zhou, S. Yang, H. Wu, Y. Wu, L. Wu, J. Pan and X. Xiong, *RSC Adv.*, 2015, **5**, 68953–68963.
59 L. Cui, X. Ding, Y. Wang, H. Shi, L. Huang, Y. Zuo and S. Kang, *Appl. Surf. Sci.*, 2017, **391**, 202–210.
60 R. Hao, G. Wang, C. Jiang, H. Tang and Q. Xu, *Appl. Surf. Sci.*, 2017, **411**, 400–410.
61 C. D. Palmer and R. W. Puls, *Natural Attenuation of Hexavalent Chromium in Ground Water and Soils, Superfund Technology Support Center for Ground Water*, Robert S. Kerr Environmental Research Laboratory, 1994.
62 J. O. Nriagu and E. Nieboer, *Chromium in the Natural and Human Environments*, 1988, vol. 20, pp. 81–104.
63 B. Sun, E. P. Reddy and P. G. Smirniotis, *Environ. Sci. Technol.*, 2005, **39**, 6251–6259.